PNAS RESEARCH ARTICLE | BIOPHYSICS AND COMPUTATIONAL BIOLOGY OPEN ACCESS

Threading single proteins through pores to compare their energy landscapes

Prabhat Tripathi[a], Arash Firouzbakht[b], Martin Gruebele[b,c,d,e,1], and Meni Wanunu[a,1]

Edited by David Baker, University of Washington, Seattle, WA; received February 15, 2022; accepted August 19, 2022

Translocation of proteins is correlated with structural fluctuations that access conformational states higher in free energy than the folded state. We use electric fields at the solid-state nanopore to control the relative free energy and occupancy of different protein conformational states at the single-molecule level. The change in occupancy of different protein conformations as a function of electric field gives rise to shifts in the measured distributions of ionic current blockades and residence times. We probe the statistics of the ionic current blockades and residence times for three mutants of the λ-repressor family in order to determine the number of accessible conformational states of each mutant and evaluate the ruggedness of their free energy landscapes. Translocation becomes faster at higher electric fields when additional flexible conformations are available for threading through the pore. At the same time, folding rates are not correlated with ease of translocation; a slow-folding mutant with a low-lying intermediate state translocates faster than a faster-folding two-state mutant. Such behavior allows us to distinguish among protein mutants by selecting for the degree of current blockade and residence time at the pore. Based on these findings, we present a simple free energy model that explains the complementary relationship between folding equilibrium constants and translocation rates.

nanopore biophysics | electric field unfolding | protein translocation | reciprocal relation | protein folding dynamics

Significance

Protein function correlates with its structural dynamics. While theoretical approaches to studying protein energy landscapes are well developed, experimental methods that enable probing these landscapes of proteins remain challenging. We used solid-state nanopores to study the translocation behavior of three mutants of a helix bundle protein and quantified the number of energetically accessible conformational states for each mutant. We found that a slower-folding mutant with access to more conformational states translocates faster than a faster-folding mutant with a smaller number of accessible states, suggesting that ease of folding and ease of translocation are at odds in this case.

Cellular proteins perform their function through a variety of pathways that have been fine-tuned over millions of years of evolution. While remarkable progress in studying protein structure at atomic resolution has been made through X-ray diffraction, NMR, and cryoelectron microscopy, more recently a new challenge has been identified: studying the dynamics of protein molecules while they interact with a complex environment, especially inside the cell (1–5). Observing such protein dynamics provides insight into the structural alterations a protein can undergo as a function of time and environmental perturbations. It is well known that proteins can undergo drastic structural changes in cells, one extreme example being protein translocation across biological compartments (6). In these cases, translocation and unfolding are intrinsically linked because the size of the pore through which a protein translocates can be comparable to or smaller than the protein itself (7). A protein typically has to deform prior to passing through the pore, which requires accessing higher free energy conformations. Various chemical changes to the protein (mutations, posttranslational modifications) can change the translocation dynamics by stabilizing/destabilizing the rate-limiting transition-state free energy (8, 9) or by optimizing the number of intermediate states (10, 11).

One way to interrogate the conformation–translocation coupling is to measure different protein conformational states at a nanopore. Nanopores in artificial lipid bilayers or in solid-state membranes have been used to analyze a wide range of macromolecules at the single-molecule level (12, 13). In these studies, interaction of a single molecule with the nanopore alters the ion flux, resulting in measurable current signals that provide information on the protein's conformation as it transits through the pore. In pioneering experiments by Kasianowicz et al. (14), it was demonstrated that ionic current blockades of single-stranded RNA oligonucleotides through the protein pore α-hemolysin were due to RNA translocation, where the mean residence time scaled linearly with the oligomer length and was inversely proportional to the applied potential. In nanopore studies of the neutral polymer polyethylene glycol, the residence time distribution was found to be single exponential, and the mean polymer residence time was inversely proportional to the voltage, indicating polymer binding/unbinding to/from the pore (15). In another pioneering work, multistep protein unfolding of the short protein thioredoxin and its unidirectional threading were demonstrated by tagging the terminus of the protein chain with an oligonucleotide (9).

Author affiliations: [a]Department of Physics, Northeastern University, Boston, MA 02115; [b]Department of Chemistry, University of Illinois at Urbana–Champaign, Champaign, IL 61801; [c]Department of Physics, University of Illinois at Urbana–Champaign, Champaign, IL 61801; [d]Beckman Institute for Advanced Science and Technology, University of Illinois at Urbana–Champaign, Champaign, IL 61801; and [e]Center for Biophysics and Quantitative Biology, University of Illinois at Urbana–Champaign, Champaign, IL 61801

Author contributions: P.T., M.G., and M.W. designed research; P.T. and A.F. performed research; P.T. and M.G. analyzed data; and P.T., A.F., M.G., and M.W. wrote the paper.

The authors declare no competing interest.

This article is a PNAS Direct Submission.

[1]To whom correspondence may be addressed. Email: mgruebel@illinois.edu or wanunu@neu.edu.

This article contains supporting information online at http://www.pnas.org/lookup/suppl/doi:10.1073/pnas.2202779119/-/DCSupplemental.

Published September 19, 2022.

Table 1. Summary of the three mutants of the λ-repressor family employed in the study, their measured folding relaxation times (19–21), and calculated dipole moments (*SI Appendix*, Fig. S1)

Mutant label	Sequence	Relaxation time (μs)	Dipole moment (Debye)
λ^{HAA}	MGSSHHHHHHSSGLVPRGSHMLTQEQLEDARRLKAIWEKKK**N**ELGLS**H**ESV**A**D KMGMGQS**AVAA**LFNGINALNAYNAALLAKILKVSVEEFSPSIAREIR	~3	158 ± 53
λ^{sA49G}	MGSSHHHHHHSSGLVPRGSHMSLTQEQLEDARRLKAIWEKKK**N**ELGLS**Q**ESV**G** DKMGMGQS**GVGG**LFNGINALNAYNAALLAKILKVSVEEFSPSIAREIR	~125	202 ± 70
λ^{N27C}	MGSSHHHHHHSSGLVPRGSHMSLTQEQLEDARRLKAIWEKKK**C**ELGLS**Y**ESV**G** DKMGMGQS**AVAA**LFNGINALNAYNAALLAKILKVSVEEFSPSIAREIR	~20	123 ± 34

Bold letters in the sequences denote the mutated residue on the Y33W pseudowild type that is the basis for all three mutants. The His tag was retained (*Materials and Methods*).

Inspired by these studies, we recently demonstrated that an electric field across a solid-state nanopore can induce excited-state conformational dynamics up to complete protein unfolding (16). In this approach, a nanoscale pore is blocked transiently by a protein molecule in its native state, and field-induced conformational fluctuations allow the protein to traverse the pore. The electric field at the nanopore constriction is used to tune the driving force, thereby allowing partially and fully unfolded conformations of cytochrome *c* to be observed by their residence time and current blockade signals. Motivated by theoretical studies (17), this approach has been further leveraged to measure fast (<1μs) transition-state passage times between protein conformational states (18).

Here, we use this approach to differentiate the energy landscape of three fast-folding mutants of λ-repressor fragment λ_{6-85} (19–21) by monitoring the characteristic ionic current blockades induced during protein translocation. Unlike cytochrome *c* (q = +8e), λ_{6-85} is more weakly charged (q = +2e), and yet, we still observed electric field–driven protein unfolding and translocation. Protein mutants can have different folding rates due to shifts in their transition-state free energies (8, 9), although mutation can also change the number of accessible (low free energy) conformational states, as predicted by the theory of minimal frustration (22). On rugged energy landscapes, downhill or two-state folding gives way to intermediates that appear during the late stages of the folding process (11). Like more conventional denaturants, temperature, or pressure (23), an electric field at the pore can bias protein molecules toward intermediate or unfolded states, and we can count individual protein conformational states as they pass through the pore.

Our measurements reveal various outcomes that depend on the applied field, including native protein dissociation from the pore and back to the bulk solution (no translocation), trapping or translocation of partially unfolded states, and complete unfolding accompanied by translocation. Measurement of translocation rates of mutants reveals protein folding/unfolding equilibria via intermediates for some mutants or simply two state for others. These single-molecule observations allow us to count the number of conformational states for each of the three λ_{6-85} mutants accessible on the timescale of our experiments, thus enabling a comparison of their energy landscapes. We find that a mutant with a greater number of low free energy intermediate states can translocate faster than a mutant with a smaller number of such states, suggesting a coupling of conformational dynamics and translocation. The unfolding energetics we observe agree with ensemble laser T-jump (19, 20) and P-jump experiments (24, 25). Regardless of the weak electrical charges of all three mutants employed in this study, we found that they can pass through a pore of diameter <3 nm without requiring chemical denaturants, a motor-driven mechanism (26, 27), or conjugation to an oligonucleotide tag (9). Finally, we demonstrate that the individual mutants in a mixture produce distinct features that allow their detection in a mixture.

Results

Protein Choice and Experimental Method. The λ-repressor is a viral protein that regulates bacteriophage lysis vs. lysogeny. Its fast folding/unfolding equilibrium facilitates observation of different states at the nanopore. Based on prior studies (19–21) by ensemble laser T-jump and P-jump experiments, we chose three mutants of λ_{6-85} with different folding relaxation times and dipole moments (Table 1) but similar radii of gyration, $R_g \sim 1.3$ nm. We selected these mutants (*SI Appendix*, section 1) because they were likely to encompass a range of numbers of folding states (20), allowing us to study their impact on the translocation dynamics. The calculated dipole moments indicated suitability for electrical unfolding experiments and hinted at a preferential orientation of the proteins along the electric field direction above a threshold field of ~20 MV/m (*SI Appendix*, section 2).

To understand the connection between protein translocation and protein conformation, we measured jumps in the ionic current due to the interaction of a protein with SiN nanopores of diameters in the range of 2 to 5 nm. Measurements were performed using a buffer comprising 1 M KCl and a 10 mM (4-2-hydroxyethyl)-piperazineethanesulfonic acid) (HEPES) buffer adjusted to pH 7.5 (*Materials and Methods* and *SI Appendix*, sections 3 and 4). Our experimental setup is illustrated in Fig. 1*A*, and example ionic current traces for λ^{HAA} at various voltages are shown in Fig. 1*B* (*SI Appendix*, section 5 has traces at other voltages). Interaction of a protein molecule with the pore reduces the ionic current through the pore by some amplitude (ΔI) from its open-pore (I_O) level. As described previously (16), the average fractional current blockade ($\Delta I/I_O$) and its duration ($\tau_{residence}$) are dependent on the protein's conformational state. For example, the unfolded state U tends to block less current and for a shorter duration than an intermediate state I or the native state N.

Monitoring the evolution of protein occupancy at the pore as a function of voltage (0 to −800 mV) or electric field ($E_{app} = V/L_{pore}$) allows us to evaluate the free energy of conformational states and extrapolate to the zero-field free energy differences between states, $\Delta\Delta G$. Measurements of $\tau_{residence}$ allow us to probe the free energy barrier ($\Delta G_j^{\ddagger Tr}$) for the translocation of a state *j* (*j* = N, I, U) (Fig. 1*C*). The native state N (the lowest free energy state in the absence of a field) of the protein is excluded from passing through the pore in our model if $d_{pore} < 3$ nm because of its very high barrier for passage. However, the intermediate state I can translocate by crossing a much lower free

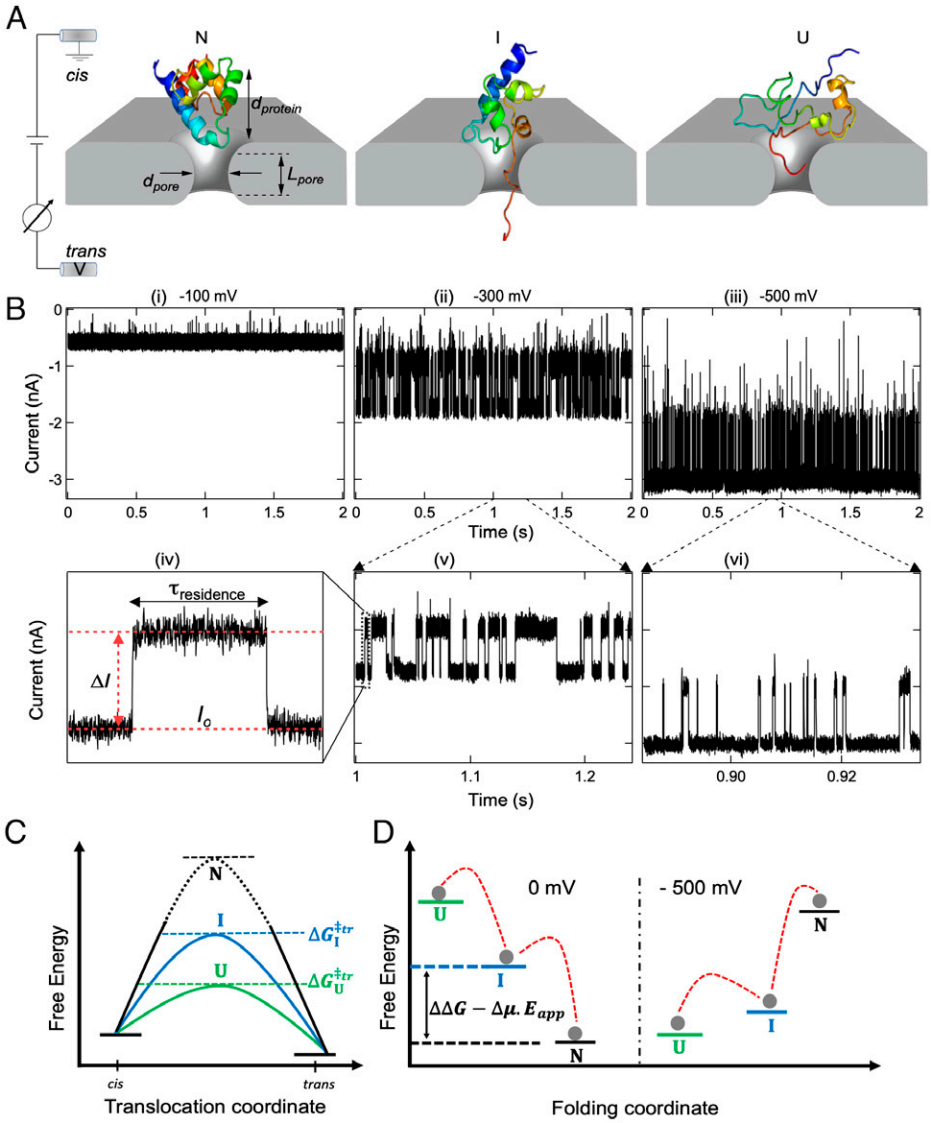

Fig. 1. Conformational occupancy during protein translocation through a solid-state nanopore. (*A*) Schematic of the experimental setup. Application of negative voltage to the trans chamber electrokinetically captures a protein molecule at the pore as it undergoes dynamic interconversion between native (N), partially unfolded intermediate (I), and unfolded (U) conformational states. (*B*) Example ionic current traces recorded for the mutant λ^{HAA} with a d_{pore} = 2.5 nm (L_{pore} = 8.8 nm) in 1 M KCl and 10 mM Hepes (pH 7.5) buffer at (*B*, *i*) −100 mV, (*B*, *ii* and *v*) −300 mV, and (*B*, *iii* and *vi*) −500 mV. (*B*, *iv*) Description of the extracted signal parameters for a typical single-molecule current blockade event. When the timescale of interconversion between states (approximately microseconds) is much faster than the residence time (milliseconds or longer) of the protein at the pore, the average value of current blockade amplitudes $\Delta I/I_O$ and its duration $\tau_{residence}$ depend on the probability of occupying conformational states N, I, and U (16). (*C*) Schematic energy diagram for translocation of protein. The energy barrier for protein translocation in state N is too high for any translocation to be detected (16) due to steric constraints, whereas translocations are detectable for the lower energy barrier states I and U. (*D*) The conformational occupancy statistics for a protein are governed by thermal excitation and the zero-field free energy difference between conformations ($\Delta\Delta G$), which is reversed by applying the external electric field ($\Delta H^{E_{app}} = -\mu . E_{app}$). Representative λ repressor conformations in *A* were picked from ∼100-μs-long molecular dynamics simulations (42).

energy barrier than state N, albeit still higher than the barrier for the unfolded state U. Upon increasing the voltage (Fig. 1*D*), U is thermodynamically stabilized, leading to shorter residence times (durations of current blockade) and reduced $\Delta I/I_O$ values. We measured $\Delta I/I_O$ and $\tau_{residence}$ for all three mutants and used clustering of the individual protein signals to evaluate the number of conformational states, the value of $\Delta\Delta G$ between states as a function of the applied field, and their $\Delta G_j^{\ddagger \mathrm{Tr}}$.

Pore Passage Detects a Low-Energy Intermediate of λ^{sA49G} Not Present in λ^{HAA}. We compared the translocation behavior of the λ^{HAA} (fastest folding) and the λ^{sA49G} (slowest folding) mutants. With a 2.5-nm-diameter pore, passage of the native state can be neglected because of the very high barrier due to steric constraints (Fig. 1*C*), and metastable intermediate states can be detected (*SI Appendix*, section 5 has λ^{HAA} and λ^{sA49G} sample traces). Capture time distributions were found to be single-exponentially distributed at all voltages for both λ^{HAA} and λ^{sA49G}, suggesting a single mode of capture at the pore for the protein molecules (*SI Appendix*, section 6).

To compare the number of intermediates on the energy landscapes of λ^{sA49G} with λ^{HAA}, we analyzed the blockade ratio ($\Delta I/I_O$) and residence time ($\tau_{residence}$) statistics for each mutant (Fig. 2). A comparison of scatterplots of $\Delta I/I_O$ vs. $\tau_{residence}$ at −250 mV is presented in Fig. 2. We see two distinct effects. Between −225 and −275 mV, a well-distinguished intermediate state is evident as a second cluster for λ^{sA49G}, whereas none is seen for λ^{HAA}. In addition, both proteins show a broadening of the main cluster in the $\Delta I/I_O$ vs. $\tau_{residence}$ distribution as a function of the electric field. The broadening could be due to

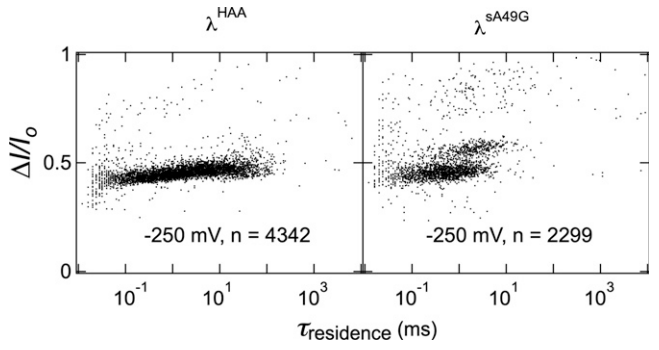

Fig. 2. Observation of intermediate states in λ^{sA49G}. Scatterplots of $\Delta I/I_O$ vs. $\tau_{residence}$ for λ^{HAA} and λ^{sA49G} mutants measured with a 2.5-nm-diameter pore at −250 mV applied voltage (the number of events [*n*] collected for each mutant is indicated). A single cluster was observed for λ^{HAA} with broadly distributed residence times, whereas for λ^{sA49G}, two clusters were observed, most likely owing to the presence of a low free energy intermediate state (in the text and Figs. 3 and 6*B*). This finding, along with a thorough analysis of the scatterplots (*SI Appendix*, section 7) and a comparison with data for a 3.5-nm-diameter pore (*SI Appendix*, section 8), suggests that at least three intermediate states are required to fully describe λ^{sA49G}, while only one intermediate is required to describe λ^{HAA} (Fig. 6*B*).

an additional intermediate state that is not fully resolved or due to the residual structure of the unfolded state that changes with the electric field (*SI Appendix*, Fig. S7*A* and section 7 have full data).

To further explore the differences among these mutants, we performed similar experiments using a larger 3.5-nm-diameter pore. A larger pore allows for the transition from lower to higher energy states to be observed directly because the barrier for passage of more folded states, which otherwise could not thread through the pore, is reduced in larger pores (*SI Appendix*, section 8 has plots). In the case of λ^{sA49G}, the ionic current fluctuates between multiple distinct levels due to transitions among several different conformational states, each blocking the pore to a different extent. λ^{HAA} shows no such flickering of currents. This can be explained by λ^{sA49G} having a rugged free energy landscape with several states within $\Delta\Delta G \sim 2\ k_BT$ separated by a low barrier, whereas λ^{HAA} has a smoother landscape consistent either with one intermediate state ~4.5 k_BT below the U state in the absence of a field (*Quantitative Free Energy Differences of Intermediate States*) or with the residual unfolded state structure that results in a broadened residence time distribution.

Quantitative Free Energy Differences of Intermediate States. The energetics of λ^{HAA} and λ^{sA49G} states can be described quantitatively by analyzing the $\Delta I/I_O$ distributions for a 2.5-nm pore (Fig. 3) and 2.0-nm pores (*SI Appendix*, Fig. S9*E* and section 9). The $\Delta I/I_O$ distributions of λ^{sA49G} required more Gaussian components than the distribution of λ^{HAA} (*SI Appendix*, section 10). To extract the energetics, we used the thermodynamic model described in our previous report (16). A three-state model was sufficient to fit the data in Fig. 3 for λ^{HAA}:

$$\left\langle \frac{\Delta I}{I_o} \right\rangle \mathrm{N} \leftrightarrow \mathrm{I} \leftrightarrow \mathrm{U} = \phi_{\mathrm{N}} P_{\mathrm{N}} + \phi_{\mathrm{I}} P_{\mathrm{I}} + \phi_{\mathrm{U}} P_{\mathrm{U}}, \qquad [1]$$

where ϕ_N, ϕ_I, and ϕ_U represent the average $\Delta I/I_O$ of states N, I, and U, respectively, and P_N, P_I, and P_U represents the probability with which each state is populated as a function of electric field E_{app}. As discussed earlier (Fig. 2), I could represent a distinct state or conformational heterogeneity of the U state. The probabilities in Eq. **1** for states j = N, I, U are given by (*SI Appendix*, section 11)

$$P_j = e^{\frac{\Delta\Delta G_{jU} - \Delta\mu_{jU} E_{app}}{k_B T}} / \mathcal{N}. \qquad [2]$$

The partition function $\mathcal{N}$ is the sum over j = N, I, U of the three exponentials in the numerator on the right-hand side of Eq. **2**. $\Delta\mu_{jU}$ is the difference in dipole moment of states

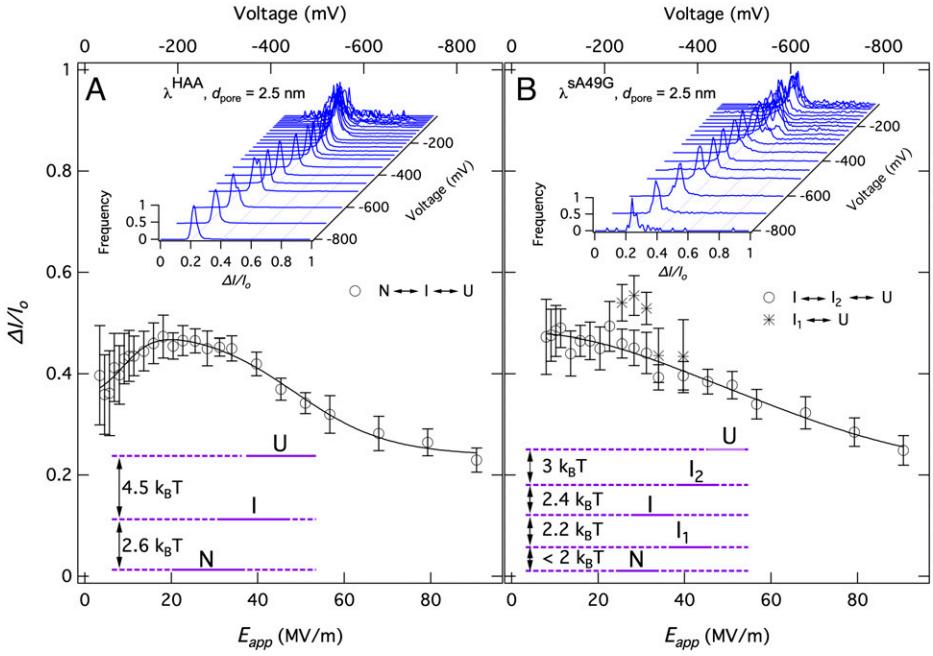

Fig. 3. Quantitative comparison of the conformational energy levels of λ^{HAA} and λ^{sA49G}. Average value of $\Delta I/I_O$ obtained from Gaussian fits to the distributions for a 2.5-nm-diameter pore (a 2-nm-diameter pore in *SI Appendix*, section S10) as a function of the electric field: (*A*) λ^{HAA} and (*B*) λ^{sA49G}. Error bars in each plot represent the SDs of the distributions obtained from the Gaussian fit. *Insets* are the distributions of $\Delta I/I_O$ as a function of voltage. The solid curve in *A* represents the fit with a three-state (N ↔ I ↔ U) model described in the text (Eq. **1**), yielding the parameters in *SI Appendix*, Table S7. The solid curve in *B* represents the fit with a three-state model I ↔ I_2 ↔ U analogous to Eq. **1**, with parameters in *SI Appendix*, Table S7. The energy level of I_1 in sA49G is evaluated from rate data (*SI Appendix*, Table S10 and section 13), and the energy level of N is estimated to be < $2k_BT$ below I_1 based on the observation that sA49G populates mostly the intermediate state for <20 MV/m.

j and U and describes the effect of the electric field on the free energy of state j, and $\Delta\Delta G_{jU}$ is the free energy difference to state U in the absence of a field. The electric field contribution to the free energy, $\Delta\mu_{jU}E_{app}$, is analogous to a denaturant–free energy change of $m[D]$ (28), where the dipole moment difference replaces the m value and the field replaces the denaturant concentration $[D]$. A similar model with additional states I_1 and I_2 was sufficient to account for the λ^{sA49G} data in Fig. 3 (*SI Appendix*, section 10 and Fig. S9*E*). At sufficiently high fields, the destabilized N state is scarcely populated; thus, we set $P_N = 0$, as evident by comparison of the $\Delta I/I_O$ distributions of $\lambda^{HAA}/\lambda^{sA49G}$ in the low–electric field regime (|Voltage| < 100 mV). This is because of the small free energy difference between N and lower energy intermediate states (Fig. 3*B*), which leads to significant destabilization of the N state even at lower electric fields, and the signal was observed due to the contributions from intermediate and unfolded states.

Fig. 3 shows the fitted $\Delta I/I_O$ distributions and mean values and a plot of the fitted zero-field free energy differences $\Delta\Delta G$ (*SI Appendix*, Table S7 shows the numerical values of $\Delta\mu_{jU}$ and uncertainties). Energy differences between the I and U states are in good agreement with reports using T-jump and ultrafast pressure jump experiments. For example, our estimated value of $\Delta\Delta G_{NI} = 2.6\ k_BT$ for λ^{HAA} is within measurement uncertainty of the 3.4 k_BT difference in the free energy of a "trap" state to the native state in ref. 25. As might be expected, we found $\phi_U < \phi_{I,N}$ (*SI Appendix*, Table S7), indicating that the unfolded state allows more ion permeation through the nanopore in comparison with the more compact I and N states, as illustrated in Fig. 1.

The Translocation Rate Increases When More Conformationally Flexible States Are Populated. We can quantitatively understand how the kinetics of translocation is tied to the energetics of unfolding by analyzing the $\tau_{residence}$ distributions measured for λ^{HAA} and λ^{sA49G}. Fig. 4*A* shows the $\tau_{residence}$ distribution of λ^{HAA} at several voltages, with dashed lines representing individual exponential probability density functions as in Sigworth and Sine (29) and solid curves representing the multicomponent distributions (*SI Appendix*, sections 12 and 13 have full data). As the electric field changes, different equilibria, such as N ↔ I or N ↔ I ↔ U, dominate the residence time distribution, and different numbers of exponentials are required to fit the distributions in Fig. 4*A*. Each exponential corresponds to an observed rate constant k_{tr}, plotted as a circle or triangle in Fig. 4*B*.

The observed rate constants k_{tr} in Fig. 4*B* can be used to fit the translocation rate constants of individual states (k_I, k_U) that have a substantial population at a given electric field (*SI Appendix*, section 13). The resulting fits are shown in Fig. 4*B* as curves. In these fits, we always ignore the fastest observed rate at low voltage, $k_{N(retraction)}$, attributed to transient blocking of the small pore by the rigid native state N rather than translocation of N. For example, the observed translocation rate constant $k_{tr}^{N\leftrightarrow I\leftrightarrow U}$ when N, I, and U are in equilibrium at the pore,

$$k_{tr}^{N\leftrightarrow I\leftrightarrow U} = P_I k_I^{N\leftrightarrow I\leftrightarrow U} + P_U k_U^{N\leftrightarrow I\leftrightarrow U}, \quad [3]$$

combines the I and U translocation rate constants weighted by the probability of each state (*SI Appendix*, section 13). In this analysis, we neglect the translocation rate contribution of the N state (i.e. k = 0) because of very larger barrier to translocation as indicated in Fig. 1C. It accounts for the observed rates (purple circles in Fig. 4*B*) between −250 and −700 mV. A simpler translocation rate model, with

$$k_{tr}^{N\leftrightarrow I} = P_I k_I^{N\leftrightarrow I}, \quad [4]$$

can account for observed rates at voltages of −125 and −250 mV when only N and I are in equilibrium and only state I translocates. In these models, P is the same probability as in Eq. **1**,

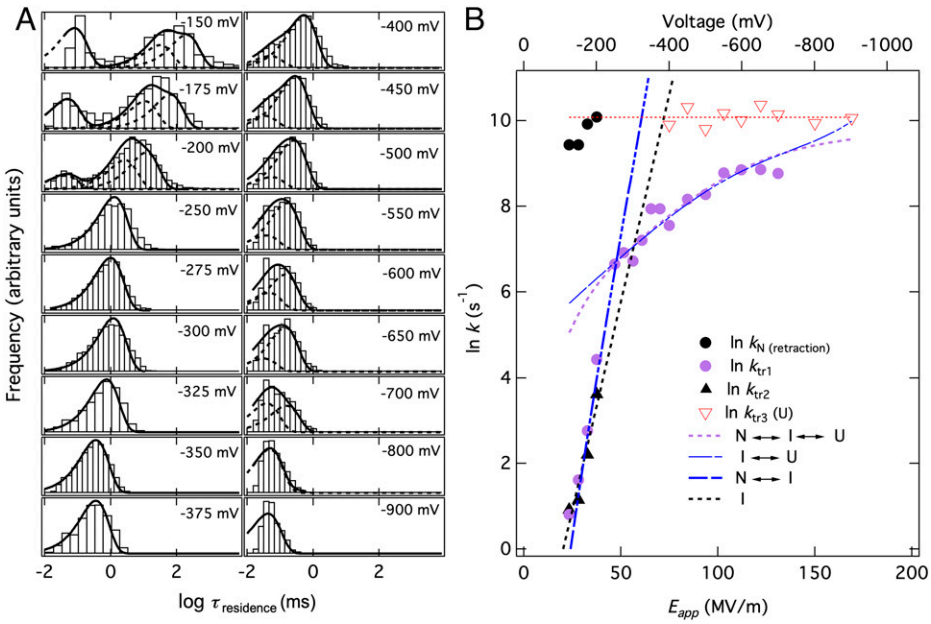

Fig. 4. Translocation rate distribution depends upon conformational probability. (*A*) Distribution of $\tau_{residence}$ of λ^{HAA} measured with a 2-nm-diameter pore as a function of voltage. One to three exponential probability density functions are required for a quantitative fit to the data at each voltage. (*B*) Observed translocation rates k_{tr} obtained from the $\tau_{residence}$ distributions at each E_{app} (voltage) for a 2-nm-diameter pore are shown as symbols. Black circles are assigned to the rate of retraction of the native state N without translocation, dominant in the low-E_{app} regime. As the electric field increases above 25 MV/m, the probability of partially (I) and fully unfolded (U) states increases, leading to an increased observed rate of translocation. Depending on the voltage and number of states populated, several models (dashed lines) are used to fit the observed translocation rates k_{tr1}, k_{tr2}, and k_{tr3} to the translocation rate constants (k_I and k_U) of individual states (*SI Appendix*, section 13 has details). Extrapolated to zero field, these fits yield zero-field translocation rates k_{0I} and k_{0U} and constants β_{0I} and β_{0U} (which reflect by how much the translocation barrier is reduced upon increasing the electric field).

and the rates are of the standard Arrhenius form $k_j = k_a \exp[-(\Delta G_j^{\dagger tr} - \beta_j E_{app})/k_B T]$, where k_a is a prefactor for translocation, $\Delta G_j^{\dagger tr}$ is the zero-field translocation barrier of the jth state as illustrated in Fig. 1*C*, and β_j is the reduction in the translocation free energy barrier upon application of the electric field in unit of MV/m.

These models, chosen to represent the nonnegligible populations of N, I, and U over the appropriate electric field ranges, account for up to three (for 2.5-nm-diameter pores) translocation rate constants k_{tr} observed experimentally (Fig. 4*B*). We found that the U state has a much faster zero-field translocation rate (*SI Appendix*, section 13) as compared with the I state in both 2.5- and 2-nm-diameter pores. Furthermore, U has a 25 times slower translocation rate in the equilibrium N ↔ I ↔ U as compared with the I ↔ U equilibrium at the higher field, which could be due to a less flexible unfolded chain at the low field (30) and/or due to additional driving force gained at the higher field because the protein refolds in the trans chamber (31). We found a larger value of β_I compared with β_U (*SI Appendix*, section 13), suggesting that the I-state structure is more sensitive to the electric field. We found a significantly slower I-state zero-field translocation rate in the 2-nm-diameter pore as compared with the 2.5-nm-diameter pore, consistent with the idea that reducing the pore diameter increases the free energy barrier for translocation.

We evaluated the λ^{sA49G} translocation rates similarly (*SI Appendix*, section 13) and extracted zero-field rates of the I-, I_2-, and U-state translocation, and we found a larger translocation rate of the U state in the sA49G mutant as compared with the λ^{HAA} mutant. This suggests that the protein with the faster folding relaxation time translocates more slowly, consistent with the notion that fast folders have stiffer unfolded chains than slow folders due to residual native-like interactions, especially so under conditions that favor the native state.

Two-State Folding of the λ^{N27C} Mutant. So far, we have studied one mutant that has several detectable intermediate states (λ^{sA49G}) and another mutant that has at most one detectable low-lying intermediate state (λ^{HAA}). In contrast to these mutants, our experiments on the λ^{N27C} mutant using pore diameters ranging from 2 to 3 nm do not reveal either any broadening or any splitting of $\Delta I/I_O$ distributions as a function of voltage (*SI Appendix*, section 14). We hypothesize that this is due to the two-state nature of λ^{N27C}, such that smaller pores of 2 to 3 nm in diameter only allow the passage of protein in the U state. Analysis of $\tau_{residence}$ distributions as above for a 3-nm-diameter pore reveals that the λ^{N27C} translocation rate as a function of E_{app} can be described by a two-state N ↔ U interconversion yielding $\Delta\Delta G_{NU} = 5.0\ k_B T$, $\Delta\mu_{NU} = 225$ Debye, and a zero-field translocation rate $k_{0U} = 416\ s^{-1}$ with $\beta_{0U} = 68$ Debye. In the presence of 2 mM oxidized glutathione [which promotes dimerization by the formation of a covalent disulfide bond between two cysteines (32)], we observed a similar distribution of $\Delta I/I_O$, suggesting that the dimerization is unlikely at low concentrations (0.5 μM) of λ^{N27C}.

To check our hypothesis of the two-state nature of λ^{N27C}, we performed experiments with 4.0- and 4.5-nm-diameter pores, slightly larger than the mean diameter of λ^{N27C} such that N ↔ U transitions on the pore can be observed directly. Experiments with a custom instrument Chimera VC100 (33, 34) capable of resolving submicrosecond current steps (33) show a clear transition in the $\Delta I/I_O$ distributions (*SI Appendix*, section 15). We performed singular value decomposition (SVD) analysis on normalized $\Delta I/I_O$ histograms (Fig. 5), revealing that two components account for >95% of the data (*SI Appendix*, section 15). These results are consistent with the apparent two-state behavior of the λ^{N27C} mutant. The second SVD basis function in Fig. 5, which monitors the voltage-dependent transition, shows a sigmoidal transition with a midpoint of −114.0 ± 0.60 mV for voltage denaturation, whereas the relative amplitude of the first component peaks prior to the midpoint of the sigmoidal transition. Such peaking has been seen in bulk experiments; while the unfolding transition is sigmoidal, the native state shows pretransition increased structural fluctuation [manifested by hyperfluorescence in bulk fluorescence studies (35)].

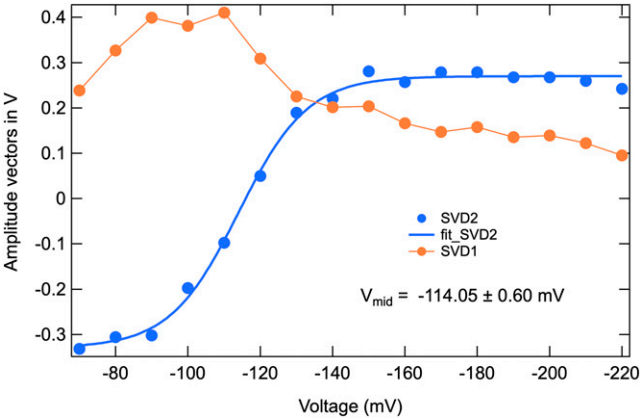

Fig. 5. Two-state characteristics of the λ^{N27C} mutant from the SVD analysis. A series of $\Delta I/I_O$ distributions similar to Fig. 3, measured for λ^{N27C} with a 4-nm-diameter pore as a function of voltage, was singular value decomposed. The filled circles show the contribution, accounting for >95% of the total signal, of the first (red) and second (blue) singular value components to $\Delta I/I_O$ as a function of voltage. The blue curve shows the N → U transition at −114 mV, and the red curve shows an increase just before the unfolding transition, analogous to the hyperfluorescence observed just before unfolding in fluorescence-detected experiments (35). *SI Appendix*, section 15 has details on the SVD analysis.

Finally, diffusion coefficients obtained from the fit with the drift–diffusion model (*SI Appendix*, section 15) are in the range of 10 to 40 $nm^2/\mu s$, 4 to 15 times smaller than the Stokes–Einstein diffusion coefficient estimated in bulk solution (~145 $nm^2/\mu s$). These values, consistent with a prior finding of smaller protein diffusion coefficients at a nanopore (34), suggest a reduced protein translational diffusivity near the pore, much like reduced diffusion due to crowding or electrostatic/hydrophobic interactions inside cells (36).

Identification of Protein Mutants in a Solution Mixture. Given the ability of solid-state nanopores to sort protein mutants by energy landscape ruggedness, we investigated if protein mutants can be identified in a solution containing a mixture of mutants λ^{sA49G}, λ^{HAA}, and λ^{N27C}. We performed experiments with a pore diameter of 3 nm and measured the ionic current blockade produced when 1) only 0.8 μM λ^{sA49G} is present in the cis (pretranslocation) chamber; 2) only 0.3 μM λ^{HAA} is present in cis; 3) 0.5 μM λ^{N27C} is present in cis; and 4) and a mixture solution containing 160 nM λ^{sA49G}, 30 nM λ^{HAA}, and 100 nM λ^{N27C} is present in cis. The scatterplots presented in Fig. 6 clearly indicate that the two-state λ^{N27C} in the solution mixture of protein mutants can be resolved. Further, we have demonstrated that resolution among the mutants can be enhanced by increasing the applied electric field (*SI Appendix*, section 16). Because λ^{HAA} translocates more slowly than λ^{sA49G}, we anticipate that these two mutants could be

separated when multiple pores are used in series. Finally, as evident in the traces in *SI Appendix*, section 16, each mutant shows a characteristic current signature, hinting at the possibility of using the current signal characteristics for resolution/separation among the mutants.

Discussion

An increasingly rugged energy landscape supports more intermediates between the unfolded state U and the native state N. Our measurements require four states to fit the data for λ^{sA49G}, three for λ^{HAA}, and two for λ^{N27C}. The ruggedness order among the mutants is, therefore, $\lambda^{sA49G} > \lambda^{HAA} > \lambda^{N27C}$ (Fig. 6*B*), different from the relaxation time order of the mutants $\lambda^{sA49G} > \lambda^{N27C} > \lambda^{HAA}$ (Table 1). In λ^{HAA}, the residual unfolded state structure or the presence of a "shallow" intermediate, which could result in the broadened residence time in Fig. 2, does not hinder its fast folding, a possibility raised in a previous report (10). On the other hand, the slower folding of λ^{sA49G} is due to greater ruggedness of its landscape (22) and a distinct intermediate in Fig. 2. In Fig. 2, the two types of intermediates are distinguished experimentally by either producing only a broadening of the $\Delta I/I_O$ and $\tau_{residence}$ distributions (λ^{HAA}) or a distinct current or lifetime cluster (λ^{sA49G}).

In contrast to folding times, the order of the translocation rate is the same as the order of the energy landscape ruggedness, $\lambda^{sA49G} > \lambda^{HAA} > \lambda^{N27C}$ (Fig. 6). Molecules with additional states low in free energy are more likely to undergo conformational fluctuations that allow them to thread through the pore faster. Thus, protein translocation is driven by conformational fluctuations. It has been proposed (37) that the translocation of disordered proteins through the bacterial cell wall is driven by entropy. The three mutants employed in our study have the same size and charge [+2e or effectively, +0.4e screened in 1 M KCl (38)], but mutants with more low-lying states have a higher conformational entropy (11). It would thus be interesting if future experiments examined the temperature dependence of translocation rates for polymers, intrinsically disordered proteins (IDPs), and ordered proteins of the same charge/size to check if it is consistent with a largely entropy-driven mechanism.

It is clear from our results here (fit to Eqs. **1**–**4**) and our previous report (16) that the electric field governs the occupancy of conformational states via the difference in their dipole moments, thus facilitating protein translocation through a narrow pore, and indeed, dipole fluctuations calculated by molecular dynamics for the three mutants (*SI Appendix*, section 17) also correlate with ruggedness and the translocation rate obtained from our nanopore experiments. In our analysis of the translocation rate of the λ^{HAA} mutant through a 2.5-nm-diameter pore (*SI Appendix*, section 13), we found different rates of U-state translocation at lower (N ↔ I ↔ U) and higher (I ↔ U only)

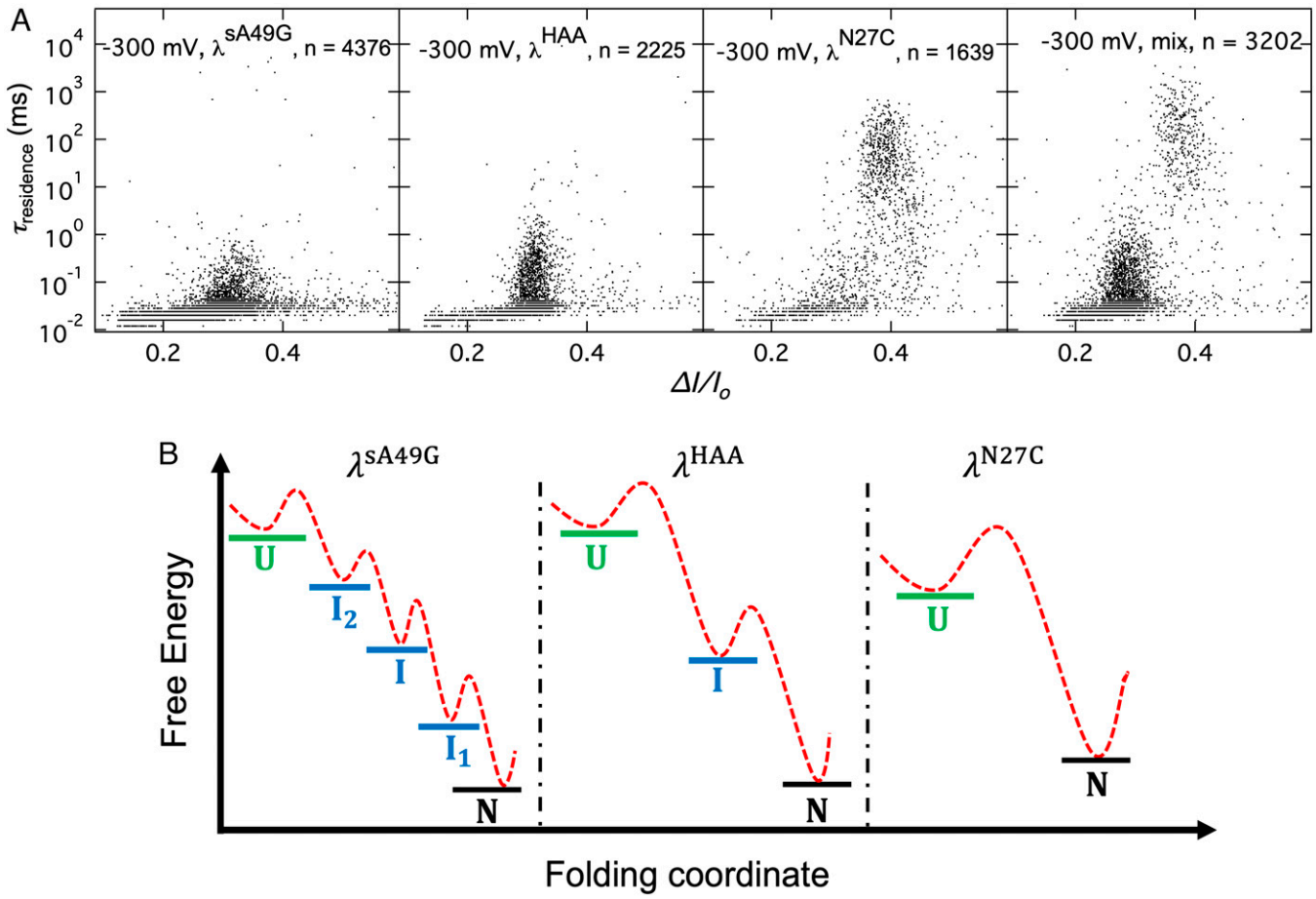

Fig. 6. Identifying mutants in a solution mixture. (*A*) Scatterplots of $\tau_{residence}$ vs. $\Delta I/I_O$ for mutants λ^{sA49G}, λ^{HAA}, and λ^{N27C} alone and a ternary mixture of all protein mutants ($V = -300$ mV, n = number of events in each experiment). These scatterplots show that the two-state λ^{N27C} mutant in the solution mixture of three protein mutants can be resolved by time/current sorting. A better separation can be achieved by changing the applied voltage (*SI Appendix*, section 16). (*B*) Summary of differences in energy landscape between the mutants. Intermediate states in λ^{HAA} and λ^{sA49G} rapidly interconvert with the unfolded state (U), which decreases the overall probability of observing protein in a fully folded state (N) and increases the overall probability of an unfolded state (and thus, the larger rate of translocation and smaller residence time) in comparison with the λ^{N27C} mutant with no intermediate.

fields. The respective fitted translocation barriers are $\Delta G_{\mathrm{U}}^{\dagger \mathrm{tr}} = 8.0\ k_B T$ under the more stabilizing low-field conditions and $4.9\ k_B T$ under the destabilizing high-field conditions. The unfolded chain is more difficult to translocate under native conditions, suggesting that it is less flexible than under unfolding conditions. Indeed, rapid cryogenic relaxation experiments probed by fluorescence, circular dichroism, and small angle X-ray scattering have shown that $\lambda_{6\text{–}85}$ collapses first to a nonnative state under stabilizing conditions (39), and single-molecule experiments on several proteins show increased friction of the unfolded state under native conditions (40). It is also possible that at the higher field, the stabilized U state gains an additional driving force for translocation by refolding to the N state in the trans chamber, as described previously (31). Thus, differences in zero-field unfolded-state translocation rates extracted from different electric field regimes indicate that posttranslocational refolding, unfolded chain stiffness, or both contributes to the translocation kinetics.

A striking feature in our data is the thermodynamic correlation between the conformational and translocation coordinates. For example, λ^{HAA} translocation through a 2.5-nm-diameter pore yields a difference $\Delta\Delta G_{\mathrm{UI}}^{\ddagger \mathrm{tr}} = \Delta G_{\mathrm{I}}^{\ddagger \mathrm{tr}} - \Delta G_{\mathrm{U}}^{\ddagger \mathrm{tr}} = 5.5\ k_B T$ (*SI Appendix*, section 13), similar to the $\Delta\Delta G_{\mathrm{IU}} = 4.5\ k_B T$ for folding obtained from the thermodynamic analysis in *SI Appendix*, Table S7 and in a previous report (20). Under the same conditions, $\Delta\beta_{\mathrm{UI}} \sim \Delta\mu_{\mathrm{IU}}$ (i.e., the analogous correlation holds between translocation and conformational kinetics) (*SI Appendix*, section 13). To understand this equivalence, one can compare the folding and translocation free energy diagrams (Fig. 1 *C* and *D*) to derive (*SI Appendix*, section 18)

$$\frac{K_{\mathrm{NI}}}{K_{\mathrm{NU}}} = \frac{k_{\mathrm{U}}^{tr}}{k_{\mathrm{I}}^{tr}} \quad \text{and} \quad \frac{k_{\mathrm{NI}}}{k_{\mathrm{NU}}} \approx \frac{k_{\mathrm{U}}^{tr}}{k_{\mathrm{I}}^{tr}}, \qquad [5]$$

where k^{tr} is the translocation rate coefficient, k is the conformational interconversion rate coefficient, and K is the conformational interconversion equilibrium constant; the second expression holds only in the special case where the U → I and I → N activation free energies are the same. Thus, there is a reciprocal relationship between equilibrium constants and translocation rates and under certain conditions, between conformational transition rates and translocation rates. This further supports the observation that the conformationally flexible mutants (i.e., having more states higher in energy than the native state) translocate more easily. It is worth noting that Eq. **3** is the electric field analog of phi-value analysis as applied to mutations (8).

As seen in Fig. 6, this propensity allows for different point mutants of the same protein to be distinguished by controlling the field at the pore and monitoring $\tau_{residence}$ vs. $\Delta I/I_O$. Further, these experiments can guide laboratory-on-a-chip protein separations performed by designing precision pores in tandem and using the device to enrich proteins in a mixture that are otherwise difficult or impossible to purify.

Materials and Methods

Protein Purification. Mutants were expressed in BL21 cells (Invitrogen) transformed by the purified plasmid encoding the His-tagged λ-repressor variant. After growth at 37 °C, harvested cells were sonicated, and protein was purified by a HisTrap column (Cytiva). His tags, which are neutral at pH 7, were not removed in accord with previous studies (41) that showed no significant change in folding times compared with proteins with His tags removed (20). Purity was assessed by sodium dodecyl sulfate-polyacrylamide gel electrophoresis (SDS-PAGE) and matrix-assisted laser desorption/ionization mass spectrometry (MALDI/MS) (*SI Appendix*, section 3 has further details, including sequence and dipole calculations).

Nanopore Experiment Conditions. We used standard methods to fabricate the silicon nitride nanopore chips and mount them in a flow cell that separates two compartments (cis and trans), each containing 1 M KCl and 10 mM HEPES (pH 7.5) buffer solution (Fig. 1*A*). To observe interactions of $\lambda_{6\text{–}85}$ mutants with a nanopore, we placed 0.03 to 0.8 μM $\lambda_{6\text{–}85}$ in the cis compartment (specific concentrations are in the figures) and applied a negative potential (−25 to −900 mV) to the trans compartment while keeping cis grounded. Additional methods are described in *SI Appendix*, section 4.

Data Acquisition and Analysis. The ionic current through nanopores was measured using an Axopatch 200B amplifier (Molecular Devices) and low-pass filtered to the indicated bandwidth using the internal Bessel filter of the Axopatch. Data points were digitized and sampled at 250-kHz sample rates on a National Instruments DAQ card using custom LabVIEW software. For the high-bandwidth measurements of ionic current (in experiments of N27C with a 4-nm-diameter pore), we used a Chimera instruments VC100 amplifier (33) (*SI Appendix*, section 4 has further details). Data fitting of $\tau_{residence}$ and $\Delta I/I_O$ distributions and their SVD decompositions were performed using custom Igor Pro software.

Data, Materials, and Software Availability. All study data are included in the article and/or *SI Appendix*.

ACKNOWLEDGMENTS. We thank D. E. Shaw Research for providing λ-repressor conformations for the schematic in Fig. 1*A*. P.T. thanks Dr. Abdelkrim Benabbas and Prof. Paul M. Champion for numerous discussions and Dr. Norman Lee and Dr. Stephan Whelan for providing access and assistance to the Circular Dichroism instrument at Boston University. P.T. and M.W. acknowledge Defense Advanced Research Projects Agency (DARPA) In Situ Phenotype Evaluation using CMOS Technology (INSPECT: Friend or Foe), as well as NIH Grant R41HG012163 for financial support. A.F. and M.G. were supported by NSF Grant MCB 2205665.

1. K. Henzler-Wildman, D. Kern, Dynamic personalities of proteins. *Nature* **450**, 964–972 (2007).
2. J. B. Stiller *et al.*, Structure determination of high-energy states in a dynamic protein ensemble. *Nature* **603**, 528–535 (2022).
3. Eyes wide open. *Nat. Chem. Biol.* **5**, 773 (2009).
4. L. M. Gierasch, A. Gershenson, Post-reductionist protein science, or putting Humpty Dumpty back together again. *Nat. Chem. Biol.* **5**, 774–777 (2009).
5. D. D. Boehr, R. Nussinov, P. E. Wright, The role of dynamic conformational ensembles in biomolecular recognition. *Nat. Chem. Biol.* **5**, 789–796 (2009).
6. W. Wickner, R. Schekman, Protein translocation across biological membranes. *Science* **310**, 1452–1456 (2005).
7. M. Karplus, J. A. McCammon, Dynamics of proteins: Elements and function. *Annu. Rev. Biochem.* **52**, 263–300 (1983).
8. A. Matouschek, J. T. Kellis Jr., L. Serrano, A. R. Fersht, Mapping the transition state and pathway of protein folding by protein engineering. *Nature* **340**, 122–126 (1989).
9. D. Rodriguez-Larrea, H. Bayley, Multistep protein unfolding during nanopore translocation. *Nat. Nanotechnol.* **8**, 288–295 (2013).
10. C. Wagner, T. Kiefhaber, Intermediates can accelerate protein folding. *Proc. Natl. Acad. Sci. U.S.A.* **96**, 6716–6721 (1999).
11. J. D. Bryngelson, J. N. Onuchic, N. D. Socci, P. G. Wolynes, Funnels, pathways, and the energy landscape of protein folding: A synthesis. *Proteins Structure* **21**, 167–195 (1995).
12. J. J. Kasianowicz, J. W. F. Robertson, E. R. Chan, J. E. Reiner, V. M. Stanford, Nanoscopic porous sensors. *Annu. Rev. Anal. Chem. (Palo Alto, Calif.)* **1**, 737–766 (2008).
13. M. Wanunu, Nanopores: A journey towards DNA sequencing. *Phys. Life Rev.* **9**, 125–158 (2012).
14. J. J. Kasianowicz, E. Brandin, D. Branton, D. W. Deamer, Characterization of individual polynucleotide molecules using a membrane channel. *Proc. Natl. Acad. Sci. U.S.A.* **93**, 13770–13773 (1996).
15. J. W. Robertson *et al.*, Single-molecule mass spectrometry in solution using a solitary nanopore. *Proc. Natl. Acad. Sci. U.S.A.* **104**, 8207–8211 (2007).
16. P. Tripathi *et al.*, Electrical unfolding of cytochrome *c* during translocation through a nanopore constriction. *Proc. Natl. Acad. Sci. U.S.A.* **118**, e2016262118 (2021).
17. R. Dutta, E. Pollak, What can we learn from transition path time distributions for protein folding and unfolding? *Phys. Chem. Chem. Phys.* **23**, 23787–23795 (2021).
18. P. Tripathi, A. Firouzbakht, M. Gruebele, M. Wanunu, Direct observation of single-protein transition state passage by nanopore ionic current jumps. *J. Phys. Chem. Lett.* **13**, 5918–5924 (2022).
19. F. Liu, M. Gruebele, Tuning λ6-85 towards downhill folding at its melting temperature. *J. Mol. Biol.* **370**, 574–584 (2007).
20. W. Y. Yang, M. Gruebele, Rate-temperature relationships in λ-repressor fragment λ 6-85 folding. *Biochemistry* **43**, 13018–13025 (2004).
21. S.-H. Chao, J. Schäfer, M. Gruebele, The surface of protein $\lambda_{6\text{-}85}$ can act as a template for recurring poly(ethylene glycol) structure. *Biochemistry* **56**, 5671–5678 (2017).

22. D. U. Ferreiro, E. A. Komives, P. G. Wolynes, Frustration in biomolecules. *Q. Rev. Biophys.* **47**, 285–363 (2014).
23. M. Boob, Y. Wang, M. Gruebele, Proteins: "Boil 'Em, Mash 'Em, Stick 'Em in a Stew." *J. Phys. Chem. B* **123**, 8341–8350 (2019).
24. M. B. Prigozhin, Y. Zhang, K. Schulten, M. Gruebele, T. V. Pogorelov, Fast pressure-jump all-atom simulations and experiments reveal site-specific protein dehydration-folding dynamics. *Proc. Natl. Acad. Sci. U.S.A.* **116**, 5356–5361 (2019).
25. M. B. Prigozhin, S.-H. Chao, S. Sukenik, T. V. Pogorelov, M. Gruebele, Mapping fast protein folding with multiple-site fluorescent probes. *Proc. Natl. Acad. Sci. U.S.A.* **112**, 7966–7971 (2015).
26. A. Depperschmidt, N. Ketterer, P. Pfaffelhuber, A Brownian ratchet for protein translocation including dissociation of ratcheting sites. *J. Math. Biol.* **66**, 505–534 (2013).
27. P. De Los Rios, A. Ben-Zvi, O. Slutsky, A. Azem, P. Goloubinoff, Hsp70 chaperones accelerate protein translocation and the unfolding of stable protein aggregates by entropic pulling. *Proc. Natl. Acad. Sci. U.S.A.* **103**, 6166–6171 (2006).
28. J. K. Myers, C. N. Pace, J. M. Scholtz, Denaturant m values and heat capacity changes: Relation to changes in accessible surface areas of protein unfolding. *Protein Sci.* **4**, 2138–2148 (1995).
29. F. J. Sigworth, S. M. Sine, Data transformations for improved display and fitting of single-channel dwell time histograms. *Biophys. J.* **52**, 1047–1054 (1987).
30. K. A. Merchant, R. B. Best, J. M. Louis, I. V. Gopich, W. A. Eaton, Characterizing the unfolded states of proteins using single-molecule FRET spectroscopy and molecular simulations. *Proc. Natl. Acad. Sci. U.S.A.* **104**, 1528–1533 (2007).
31. I. Drobnak, E. Braselmann, P. L. Clark, Multiple driving forces required for efficient secretion of autotransporter virulence proteins. *J. Biol. Chem.* **290**, 10104–10116 (2015).
32. D. L. Nelson, *Lehninger Principles of Biochemistry* (W. H. Freeman, New York, NY, ed. 4, 2005).
33. J. K. Rosenstein, M. Wanunu, C. A. Merchant, M. Drndic, K. L. Shepard, Integrated nanopore sensing platform with sub-microsecond temporal resolution. *Nat. Methods* **9**, 487–492 (2012).
34. J. Larkin, R. Y. Henley, M. Muthukumar, J. K. Rosenstein, M. Wanunu, High-bandwidth protein analysis using solid-state nanopores. *Biophys. J.* **106**, 696–704 (2014).
35. J. Ervin, E. Larios, S. Osváth, K. Schulten, M. Gruebele, What causes hyperfluorescence: Folding intermediates or conformationally flexible native states? *Biophys. J.* **83**, 473–483 (2002).
36. M. Guo, H. Gelman, M. Gruebele, Coupled protein diffusion and folding in the cell. *PLoS One* **9**, e113040 (2014).
37. D. K. Halladin *et al.*, Entropy-driven translocation of disordered proteins through the Gram-positive bacterial cell wall. *Nat. Microbiol.* **6**, 1055–1065 (2021).
38. M. Muthukumar, Communication: Charge, diffusion, and mobility of proteins through nanopores. *J. Chem. Phys.* **141**, 081104 (2014).
39. S. J. Kim, Y. Matsumura, C. Dumont, H. Kihara, M. Gruebele, Slowing down downhill folding: A three-probe study. *Biophys. J.* **97**, 295–302 (2009).
40. A. Soranno *et al.*, Quantifying internal friction in unfolded and intrinsically disordered proteins with single-molecule spectroscopy. *Proc. Natl. Acad. Sci. U.S.A.* **109**, 17800–17806 (2012).
41. M. B. Prigozhin *et al.*, Reducing lambda repressor to the core. *J. Phys. Chem. B* **115**, 2090–2096 (2011).
42. K. Lindorff-Larsen, S. Piana, R. O. Dror, D. E. Shaw, How fast-folding proteins fold. *Science* **334**, 517–520 (2011).